Theor Chem Acc (2017) 136:51
DOI 10.1007/s00214-017-2082-2

REGULAR ARTICLE

Electronic structure and rearrangements of anionic $[ClMg(\eta^2\text{-}O_2C)]^-$ and $[ClMg(\eta^2\text{-}CO_2)]^-$ complexes: a quantum chemical topology study

Mónica Oliva[1] · Vicent S. Safont[1] · Patricio González-Navarrete[1] · Juan Andrés[1]

Received: 10 January 2017 / Accepted: 12 March 2017 / Published online: 20 March 2017

Abstract The electronic structure and rearrangements of anionic $[ClMg(\eta^2\text{-}O_2C)]^-$ and $[ClMg(\eta^2\text{-}CO_2)]^-$ complexes have been elucidated by the combined use of bonding evolution theory, quantum theory of atoms in molecules, and non-covalent interaction index. The results obtained from this quantum chemical topological study allow identifying the evolution of strong and weak interactions among Mg, O, and C atoms, as well as the origin of the preference of the system for a determined reaction pathway, recovering the electron flow and bonding patterns along the reaction pathways connecting these complexes.

Keywords Bonding evolution theory · Non-covalent interactions · Quantum theory of atoms in molecules · $[ClMg(\eta^2\text{-}O_2C)]^-$ complex · $[ClMg(\eta^2\text{-}CO_2)]^-$ complex

1 Introduction

Carbon dioxide (CO_2) is viewed as an optimal C-1 source in organic synthesis owing to its abundance, availability, and low cost [1–10]. Likewise, its conversion into more added value chemicals is currently receiving special attention due to the significant increase in CO_2, one of the most important causes directly linked to climate change. In this sense, the excessive production of CO_2 has been recognized as one of the greatest environmental threats of our times [11], and therefore, it is of crucial importance to reduce the CO_2 accumulation in the atmosphere in order to mitigate its increasing buildup.

Chemical fixation of CO_2 by metal complexes has gained an increasing attention and has been currently studied at length, even at a strictly molecular level [12–16], but it still represents at the present time one of the most relevant issues, while improvements in the feasibility of using CO_2 as a carbon feedstock in chemical synthesis are being currently carried out [4, 10]. In this context, magnesium complexes are highly promising materials since they combine the possibility to produce, through (photo)catalytically driven reactions, raw materials, and valuable chemicals, together with a substantial mitigation of the greenhouse effect [17–28], as well as play an important role in carbon–carbon bond forming reactions [29–31]. However, despite considerable efforts to develop structure–reactivity relationships, the actual reaction mechanisms of such magnesium oxide complexes are still controversial [32]. A complete understanding of the coordination of CO_2 to the Mg is essential in order to give some insights into the reactivity toward CO_2 activation.

The most common coordination of CO_2 in neutral and anionic complexes containing a single metal atom has been found to be monodentate $M(\eta^1\text{-}CO_2)$ and bidentate $M(\eta^2\text{-}CO_2)$ [4, 33–36], whereas cationic species have shown to exclusively have a linear "end-on" coordination $[M\text{-}(CO_2)_n]^+$ [37–43]. Recently, Miller et al. [44] have identified a bidentate double-oxygen metal–CO_2 coordination magnesium complex $[ClMg(\eta^2\text{-}O_2C)]^-$ that has not been previously observed neither in neutral nor in charged unimetallic complexes. In this study, the evidence of a bidentate double-oxygen magnesium complex

Published as part of the special collection of articles derived from the 10th Congress on Electronic Structure: Principles and Applications (ESPA-2016).

✉ Mónica Oliva
oliva@uji.es

[1] Departamento de Química Física y Analítica, Universitat Jaume I, Avda. Sos Baynat s/n, 12071 Castelló de la Plana, Spain

$[ClMg(\eta^2\text{-}O_2C)]^-$ has been supported by infrared photodissociation spectroscopy and quantum chemical calculations, where exploration of potential energy surfaces (PESs) for the obtaining of the $[ClMg(\eta^2\text{-}O_2C)]^-$ complex has been carried out. Motivated by these results, we present herein in greater detail the analysis of the electronic structure and rearrangements of both anionic $[ClMg(\eta^2\text{-}O_2C)]^-$ and $[ClMg(\eta^2\text{-}CO_2)]^-$ complexes.

For a detailed analysis of a chemical system, relevant intermediates and transition states are identified according to their relative energies. Within this context, the direct analysis of the wave function that is an eigenstate of an electronic Hamiltonian provides the complete information about these stationary structures and thus of the geometry and electronic structure of the system. However, the wave function is an extremely complex mathematical function, which depends on the positions and spins of all the electrons; therefore, analyzing details or comparing many-electron wave functions is a demanding task owing to various practical difficulties. To overcome this inconvenience, the molecular orbital theory or the valence bond theory is used in an attempt to connect with classical chemical concepts such as chemical bond, electron pair, or Lewis structure. Another procedure is to condense the relevant information into a single three-dimensional function of space, a scalar field, and describe chemical reactivity based on well-defined physical entities accessible from experiments. This strategy belongs to the framework of quantum chemical topology (QCT) [45], a subarea of quantum mechanics providing a rigorous and exact definition of bonding within an atomic ensemble in terms of topological properties of different scalar fields that yields a wealth of calculated chemical information from the wave function of a molecule.

In the present work, three procedures are employed to characterize the electronic structures and rearrangements of both anionic $[ClMg(\eta^2\text{-}O_2C)]^-$ and $[ClMg(\eta^2\text{-}CO_2)]^-$ complexes: the bonding evolution theory (BET), proposed by Krokidis and Silvi [46–50] which combines the topological analysis of the electron localization function (ELF) [51, 52] and Thom's catastrophe theory (CT); [53] the topological analysis of the electron density in the framework of the quantum theory of atoms in molecules (QTAIM) [54]; and the non-covalent interaction (NCI) index [55]. NCI approach has shown great success for visualizing weak interactions and enabling the characterization of both stabilizing (hydrogen bonds, van der Waals) and destabilizing (steric clashes) interactions in different molecules and materials [56–60]. The combination of these procedures has become very insightful for probing the electronic structure, and constitutes a powerful tool in the study of chemical events, providing new strategies to understand and visualize the electron flow along the molecular mechanisms of chemical rearrangements.

This paper is organized as follows: The theoretical procedures and computational procedures are described in Sect. 2. In the following section, the results are presented and discussed, and finally the conclusions section provides a summary of the work and concluding remarks.

2 Computational procedures

Quantum chemical calculations have been performed using the Gaussian 09 program [61]. We have selected the B3LYP [62, 63] exchange–correlation functional and the 6-311++G** basis set for the geometry optimizations. Vibrational frequencies were calculated to characterize the structures as minimum or transition states (TSs) as well as to obtain the zero-point energy corrections. Afterward, the intrinsic reaction coordinate (IRC) [64, 65] pathway was traced to their corresponding associated reactants and products. A mass-weighted step of 0.05 $amu^{1/2}$ bohr has been employed until the minimum was reached. For each point along the IRC, the wave function has been obtained and the ELF analysis has been performed by means of the TopMod09 package [66] considering a cubical grid of stepsize smaller than 0.05 bohr. The ELF basins are visualized using the program Chimera [67]. The topological partition of the ELF gradient field [52] provides basins of attractors, which are classified as core and valence basins. Core basins C(A) can be thought as atomic cores, while valence basins V(A) can be interpreted as bond and lone pairs, where A is the atomic symbol of the element. V(A), V(A,B), or V(A,B,C) are characterized by their coordination number with core basins (synaptic order) as monosynaptic, disynaptic or trisynaptic basins, respectively [68].

Along a reaction pathway (which links the chemical structures and therefore the topologies of the ELF gradient fields of the reactants with those of the products), the system experiences a series of structural stability domains (SSDs) within which all the critical points are hyperbolic separated by catastrophic points at which at least one critical point is non-hyperbolic. The bifurcation catastrophes occurring at these turning points are identified according to Thom's classification [53] which gives access to their unfolding, a compact polynomial expression which contains all the information about how ELF may change as the control parameters change. In this way, a chemical reaction is viewed as a sequence of elementary chemical processes characterized by a catastrophe. These chemical processes are classified according to the variation in the number of basins μ and/or of the synaptic order σ of at least one basin. Some reviews on the ingredients and applicability of BET to understand and rationalize chemical structure and reactivity have been discussed and scrutinized in more detail [47, 69–71].

Topological analysis of the electron density obtained by QTAIM is done by using the program Multiwfn [72]. QTAIM, a model based on quantum mechanics and physical observables, provides a rigorous and exact definition of bonding within an atomic ensemble in terms of topological properties of its charge density. In addition, NCI is a topological tool to visualize non-covalent interactions [73], providing rich representations of a range of attractive and repulsive interactions. The NCI scheme is based on the so-called reduced density gradient s(ρ) function, which is defined using the electron density, ρ, and its first derivatives as follows:

$$s(\rho) = \frac{1}{2(3\pi^2)^{1/3}} \frac{|\nabla\rho(r)|}{\rho(r)^{4/3}}$$

where $\rho(r)$ is the electron density. In density tails (i.e., regions far from the molecule, in which the density is decaying to zero exponentially), the reduced gradient has very large positive values. On the contrary, the $s(\rho)$ function assumes very small values, approaching zero, for regions of both covalent bonding and non-covalent interactions. By multiplying the density by the sign of the second eigenvalue of the density Hessian (λ_2), one can distinguish the strength and the attractive or repulsive nature of the interactions [57]. A characterization of places where the non-covalent interactions play an essential role in a molecule stems from the experimental observations that such interactions may be responsible for the course of the chemical reactions [56]. Likewise, the density critical point (CP) that occurs between weak inter- or intramolecular interactions induces dramatic changes in the $s(\rho)$ plot [59]. Since the behavior of $s(\rho)$ at low densities is dominated by $\rho(r)$, $s(\rho)$ tends to diverge except in the regions around a density CP, where the density gradient dominates, and $s(\rho)$ approaches zero.

3 Results and discussion

In the present study, we have characterized the formation processes of both $[ClMg(\eta^2\text{-}O_2C)]^-$ and $[ClMg(\eta^2\text{-}CO_2)]^-$ complexes (**P-A** and **P-B,** respectively, see Fig. 1) from an oxalic acid and a magnesium salt complex (**R**). Likewise, we have performed the topological analysis of the electron density under the domain of the BET, QTAIM, and the NCI index in order to describe the evolution of the topology of these three gradient fields.

3.1 Energy and geometry description

The results obtained from the exploration of the PESs have been found in line with those previously reported by Miller et al. [44]. The calculated energy profile involving the formation processes of both $[ClMg(\eta^2\text{-}O_2C)]^-$ (**P-A**) and $[ClMg(\eta^2\text{-}CO_2)]^-$ (**P-B**) complexes from oxalic acid and a magnesium salt complex (**R** and **R′**) is depicted in Fig. 1. The exploration of the PES for the formation of **P-A** reveals that **TS-A** is predicted to be 32.8 kcal mol^{-1} above

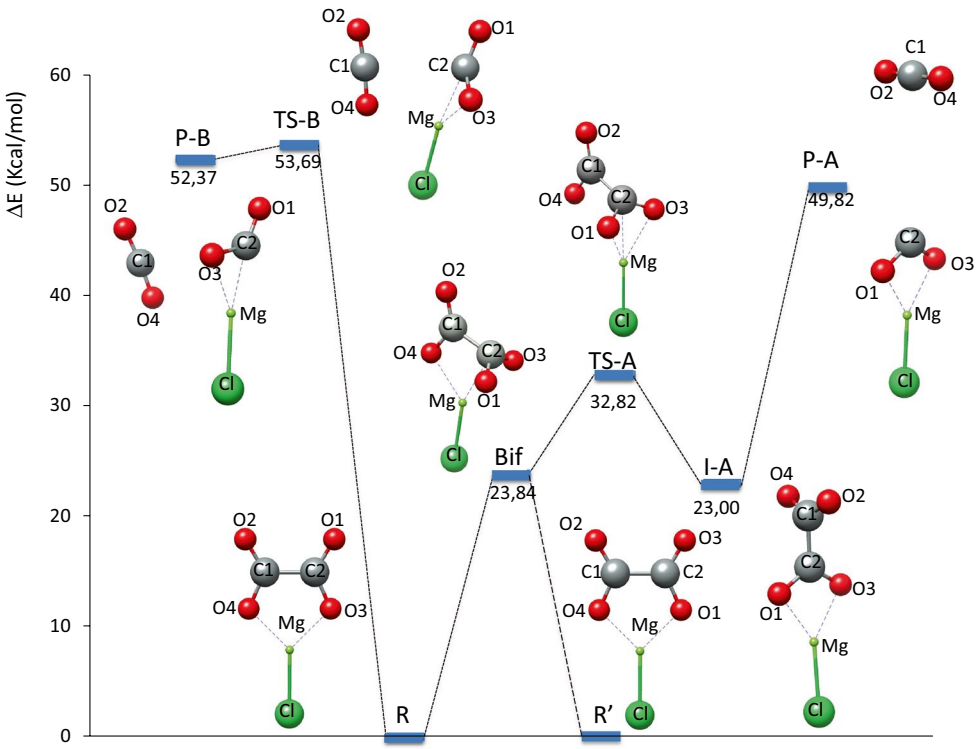

Fig. 1 Potential energy profile (including the zero-point energy correction) and geometries of the stationary points for A and B mechanisms, leading to the bidentate double-oxygen complex $[ClMg(\eta^2\text{-}O_2C)]^-$ (**P-A**), and bidentate carbon oxygen complex $[ClMg(\eta^2\text{-}CO_2)]^-$ (**P-B**). Relative energies (in kcal mol^{-1}) to reactants (**R**)

the line of the oxalic complex **R** or **R′** and clearly more favored than **TS-B**. **TS-A** has been characterized by means of a unique imaginary vibrational mode that is mainly associated with the stretching of O4–Mg bond. In addition, a detailed exploration of the PES reveals the appearance of a bifurcation point (**Bif**) along the path connecting **TS-A** and **R** and **R′**. The presence of **Bif** was confirmed by means of IRC calculations and corresponds to the link between the species **R** or **R′** due to the rotation of the torsion angle O4–C1–C2–O1; this species is predicted to be 23.8 kcal mol^{-1} higher in energy than **R** or **R′**. Likewise, the relaxation of **TS-A** in an opposite way gives rise to the formation of the intermediate **I-A**. This species is calculated to be 23.0 kcal mol^{-1} higher than **R** complex, while this rearrangement entails a change in the coordination of the metal center; in particular, Mg atom interacts now with O1 and O3. Certainly, this change in the coordination prepares the system for the imminent C–C dissociation in order to give rise to the formation of the bidentate double-oxygen complex interacting with CO_2 (**P-A**). It is worth noting that the formation of **P-A** from **I-A** does not entail a thermal process, and therefore, the system needs to invest 26.8 kcal mol^{-1} to reach **P-A**, and the subsequent liberation of products: the bidentate complex [ClMg(η^2-O_2C)]$^-$ + CO_2. Note that the liberation of the final products from **P-A** is predicted slightly endothermic (only 0.5 kcal mol^{-1}).

On the other hand, the alternative route to reach the bidentate complex [ClMg(η^2-CO_2)]$^-$ is obtained via **TS-B**, which is predicted to be 53.7 kcal mol^{-1} higher in energy than **R** complex and certainly less favored than the reaction pathway via **TS-A**. Subsequently, **TS-B** gives rise to the formation of the product complex **P-B** which is predicted to be only 1.4 kcal mol^{-1} more stable than **TS-B** and where the CO_2 molecule weakly interacts with the [ClMg(η^2-CO_2)]$^-$ moiety. Finally, the liberation of the final products ([ClMg(η^2-CO_2)]$^-$ + CO_2) from **P-B** is predicted to be endothermic by 2.6 kcal mol^{-1}.

3.2 Topological description

3.2.1 Formation of the [ClMg(η^2-CO_2)]$^-$ complex

The BET analysis of the reaction pathway for the formation of the [ClMg(η^2-CO_2)]$^-$ complex has been carried out. The evolution of the basin populations for some ELF attractors along the IRC is depicted in Fig. 2, and the respective snapshots of their corresponding SSDs for some selected points on the IRC path are depicted in Fig. 3. QTAIM and NCI analyses have been also performed in order to complement the BET analysis.

At **R** complex, the basins localized are (see Fig. 3): 8 core basins (purple buttons), 5 disynaptic basins (green buttons) accounting for the C–C and C–O bonds, and 11 monosynaptic basins (red buttons) accounting for the oxygen and chlorine lone pairs. For the sake of clarity, the monosynaptic basin populations of each O atom have been unified as a unique basin population, i.e., $V_{i=1,2\ldots}(X_i) = V(X_i)$. In addition, due to the low and positive values of the electron density and its Laplacian, respectively, at

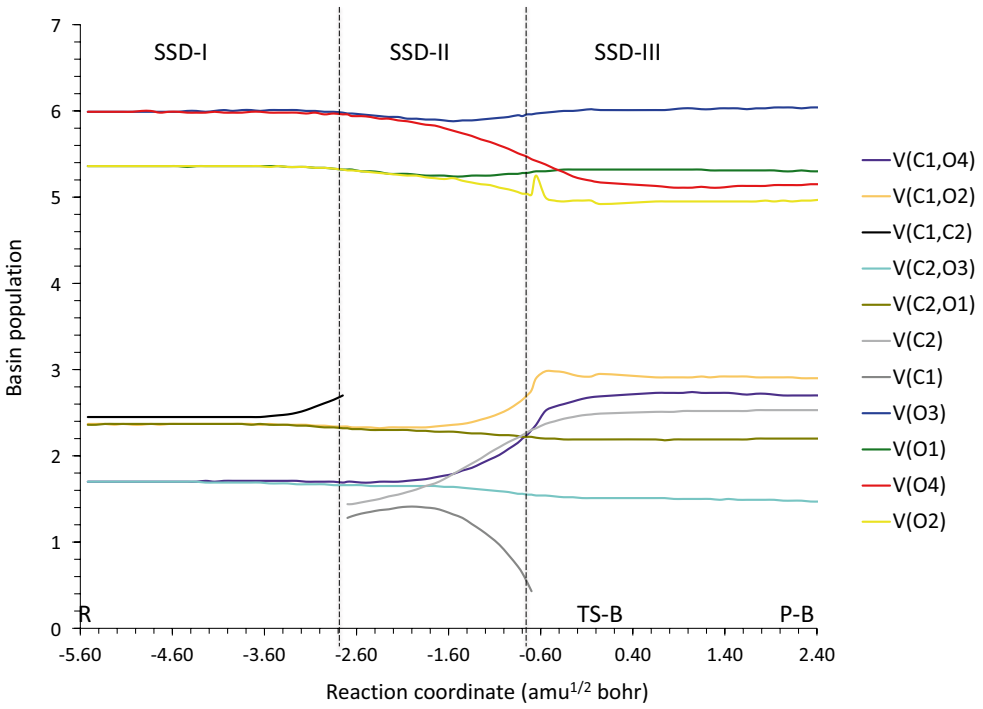

Fig. 2 Evolution of the populations of some basins along the IRC pathway for the formation of **P-B** as a function of the reaction coordinate (amu$^{1/2}$ bohr). Dashed lines separate the three structural stability domains (SSD). For the sake of clarity, the valence basin populations of oxygen atoms have been unified as a unique basin population, i.e., $V_{i=1,2\ldots}(X_i) = V(X_i)$

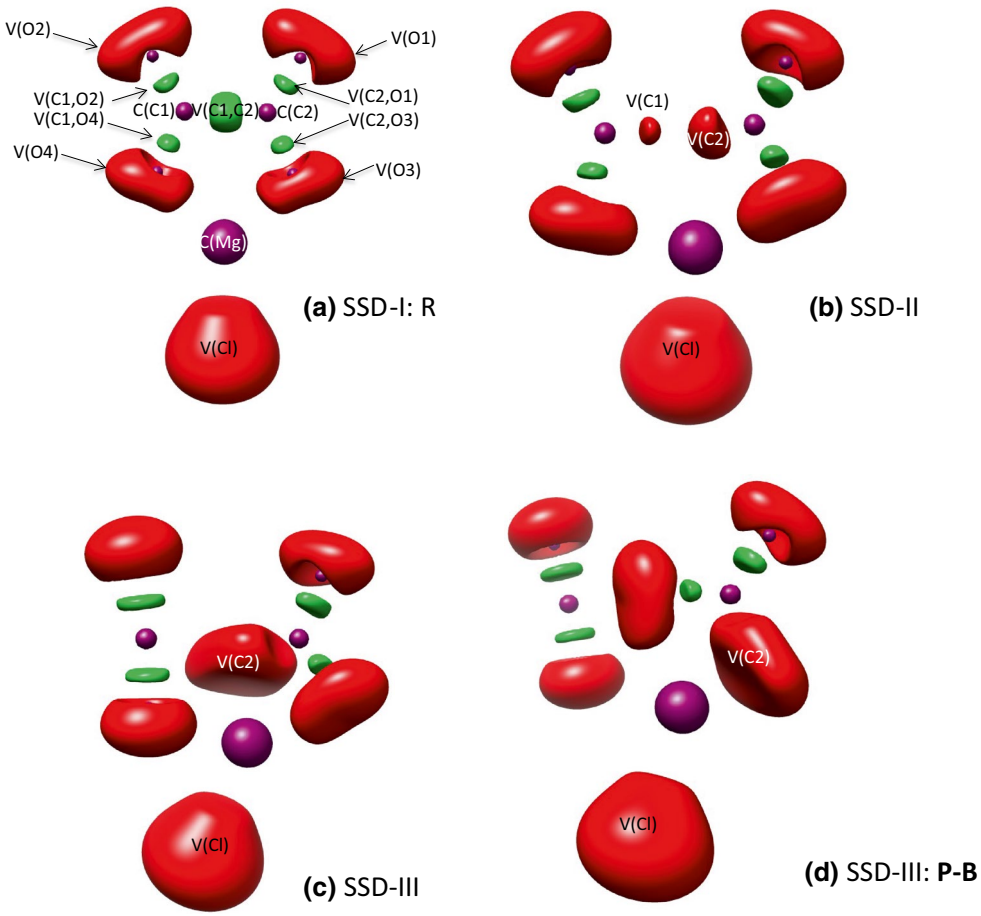

Fig. 3 Snapshots of the ELF localization domains for selected points along the IRC for the formation of **P-B**. The isosurface value is $\eta = 0.814$. The reaction coordinate value is **a** $s = -5.519$ amu$^{1/2}$ bohr, **b** $s = -1.499$ amu$^{1/2}$ bohr, **c** $s = -0.050$ amu$^{1/2}$ bohr, **d** $s = 2.591$ amu$^{1/2}$ bohr. The *color code* is as follows: *green* disynaptic basins; *red* monosynaptic basins; *purple* core basins

their corresponding bond critical points (BCPs) (3,−1), the system suggests "closed-shell" interactions among Mg–O3, Mg–O4, and Mg–Cl bonds (see Table 1a). This is also corroborated by the NCI index; Fig. 4a shows the strong attractive interaction, blue in color and very disk-shaped between Mg–Cl, Mg–O3, and Mg–O4 atoms; this is a very localized interaction which expands from the corresponding BCPs [59]. Moreover, a second weak interaction is observed from the green isosurface at the center of the ring formed by C1–C2–O3–Mg–O4 atoms which is related to the ring critical point (RCP) localized in the QTAIM analysis.

The BET analysis of this chemical rearrangement reveals three well-established chemical events (or structural stability domains, SSDs) associated with two topological changes. Starting from the **R** complex, the first topological change in the ELF field accounts for a cusp-type catastrophe which connects SSD-I and SSD-II, where the disynaptic basin V(C1,C2) splits into two monosynaptic basins V(C1) and V(C2) (see Figs. 2, 3). Interestingly, the V(C1,C2) basin collapses and splits into two new monosynaptic basins due to an excess of charge density, whereas the rest of the basin populations remain almost unaltered (see Figs. 2, 3b). The QTAIM analysis at the first point of the SSD-II also accounts for the breaking process of the C1–C2 bond (see Table 1b). For instance, small value of electron density $\rho(r_{BCP})$, positive value of the Laplacian (r_{BCP}), and negative energy density $E^e(r_{BCP})$ at the (3,−1) BCP confirm the breaking process of C1–C2 bond. Likewise, the NCI analysis also accounts for week interactions (depicted in blue in Fig. 4b) between C1 and C2 atoms.

The main factors observed in the course of the SSD-II is the steady increase in the population of the monosynaptic basin V(C2), while the population of the monosynaptic basin V(C1) decreases as the reaction proceeds. At the same time, the population of the disynaptic basins V(C1,O2) and V(C1,O4) grow (this is even emphasized at the end of the SSD-II) giving rise to the imminent liberation of CO_2 molecule. The SSD-II finishes with the annihilation of the monosynaptic basing V(C1) giving rise to the last SSD-III. A fold type of catastrophe accounts for the annihilation of the monosynaptic basin V(C1); in contrast, the presence of the monosynaptic basin V(C2) in the course of SSD-III reveals the strong carbene character of the complex $[ClMg(\eta^2\text{-}CO_2)]^-$ which is supported by the considerably augmented population of the monosynaptic basin V(C2) (~2.5e) at the end of this SSD. Likewise, it

Table 1 Values of the electron density $\rho(r_{BCP})$, potential energy density $V(r_{BCP})$, kinetic energy density $G(r_{BCP})$, Laplacian of the electron density $\nabla^2\rho(r_{BCP})$, and electronic energy density $E^e(r_{BCP})$ at the (3,−1) BCPs

Bond	$\rho(r_{BCP})$	$V(r_{BCP})$	$G(r_{BCP})$	$\nabla^2\rho(r_{BCP})$	$E^e(r_{BCP})$
(a) R complex					
Mg–Cl	0.044	−0.055	0.057	0.237	0.002
Mg–O3	0.055	−0.082	0.096	0.430	0.014
Mg–O4	0.055	−0.082	0.096	0.430	0.014
C1–O4	0.326	−0.858	0.366	−0.501	−0.492
C2–O3	0.326	−0.858	0.366	−0.501	−0.492
C2–O1	0.407	−1.326	0.639	−0.185	−0.687
C1–O2	0.407	−1.326	0.639	−0.185	−0.687
C1–C2	0.223	−0.208	0.047	−0.458	−0.161
(b) SSD-II					
Mg–Cl	0.044	−0.054	0.056	0.234	0.002
Mg–O3	0.049	−0.070	0.082	0.380	0.012
Mg–O4	0.042	−0.055	0.067	0.313	0.012
C2–O3	0.337	−0.920	0.402	−0.463	−0.518
C1–O4	0.365	−1.067	0.483	−0.399	−0.584
C1–C2	0.047	−0.017	0.011	0.020	−0.006
C2–O1	0.410	−1.385	0.693	0.005	−0.692
C1–O2	0.420	−1.442	0.726	0.043	−0.715
(c) SSD-III					
Mg–Cl	0.042	−0.050	0.052	0.215	0.002
Mg–O3	0.050	−0.073	0.086	0.394	0.013
Mg–O4	0.012	−0.011	0.013	0.588	0.002
C2–O3	0.306	−0.761	0.315	−0.521	−0.446
Mg–C2	0.043	−0.057	0.058	0.241	0.001
C2–O1	0.446	−1.535	0.752	−0.124	−0.783
C1–O4	0.398	−1.302	0.642	−0.069	−0.660
C1–O2	0.461	−1.658	0.837	0.069	−0.820
(d) P-B					
Mg–Cl	0.042	−0.050	0.052	0.214	0.002
Mg–O3	0.048	−0.070	0.082	0.378	0.012
Mg–C2	0.022	−0.059	0.060	0.244	0.001
C2–O3	0.299	−0.721	0.293	−0.537	0.428
C1–O3	0.015	−0.011	0.012	0.055	0.001
C2–O1	0.399	−1.312	0.648	−0.059	0.664
C1–O4	0.449	−1.554	0.763	−0.105	0.791

is important to note that **TS-B** has been localized along the SSD-III; nevertheless, the rupture of the C1–C2 bond from the ELF point of view takes place at an earlier stage of the process (in particular in the SSD-II), and therefore, **TS-B** only plays a role from the energetic description. In addition, both QTAIM and NCI analyses for **P-B** show the presence of weak interactions between the CO_2 molecule and the $[ClMg(\eta^2\text{-}CO_2)]^-$ moiety, which is reflected in the localized (3,−1) BCP between C1 and O3 atoms accounting for a "closed-shell" interaction (for details, see Table 1d); in addition, the NCI analysis also reveals this weak type of interaction which is reflected as a green isosurface dividing the complex **P-B** into two fragments. Moreover, QTAIM and NCI show and coincide that the interaction between C2 and O3 with Mg in the $[ClMg(\eta^2\text{-}CO_2)]^-$ moiety lacks covalent character, although strong interactions in blue are sensed from the NCI analysis; these were predicted at values of the electron density close to zero. Consequently, the absence of disynaptic basins V(C2,Mg) and V(O3,Mg) also corroborates this response from the system (for details, compare Table 1d and Fig. 4d).

3.2.2 *Formation of the $[ClMg(\eta^2\text{-}O_2C)]^-$ complex*

The evolution of the ELF field shows that there are not topological changes in the sequence **R** → **Bif** → **TS-A** → **I-A**. Actually, the same type and number of basins have been found in all these species in spite of the important geometrical rearrangements involved in this step (see Fig. 1). The absence of breaking/forming processes only accounts for the change in the coordination of the magnesium atom. Thus, the evolution of the basin populations from **R** to **I-A** just reveal minor modifications in the populations of monosynaptic basins (V(O1), V(O2), V(O3), V(O4)) and disynaptic basins (V(C1,O4), V(C1,O2), V(C1,C2), V(C2,O3) V(C2,O1)). Likewise, the transformation of **R** into **R′** via **Bif** does not account for any topological change since the type of interactions involved in **R′** is exactly the same as those found in **R**, and therefore, **R′** does not entail any special feature as compared to **R**.

As stated above, the transformation of **I-A** into **P-A** cannot be conceived as a thermal process; a photodissociation would have been required for the subsequent formation of **P-A**. Consequently, no reaction pathway was traced to characterize the final step of this chemical rearrangement; therefore, we have characterized just the final intermediate **P-A** in order to complete the topological analysis. After the photodissociation process, the topological evolution of the ELF results in a similar distribution of ELF basins (see Fig. 5) as obtained for the formation of **P-B**, i.e., transformation of the disynaptic basin V(C1,C2) into the monosynaptic basin V(C2) with the concomitantly annihilation of the monosynaptic basin V(C1). Despite the similar ELF topology that presents **P-A** and **P-B**, the spatial distribution of their monosynaptic basins V(C2) is rather dissimilar making these two carbene species considerably different in terms of their chemical reactivity due to the orientation of the monosynaptic basin V(C2). Note that the carbene character of species **P-B** has been experimentally observed [44].

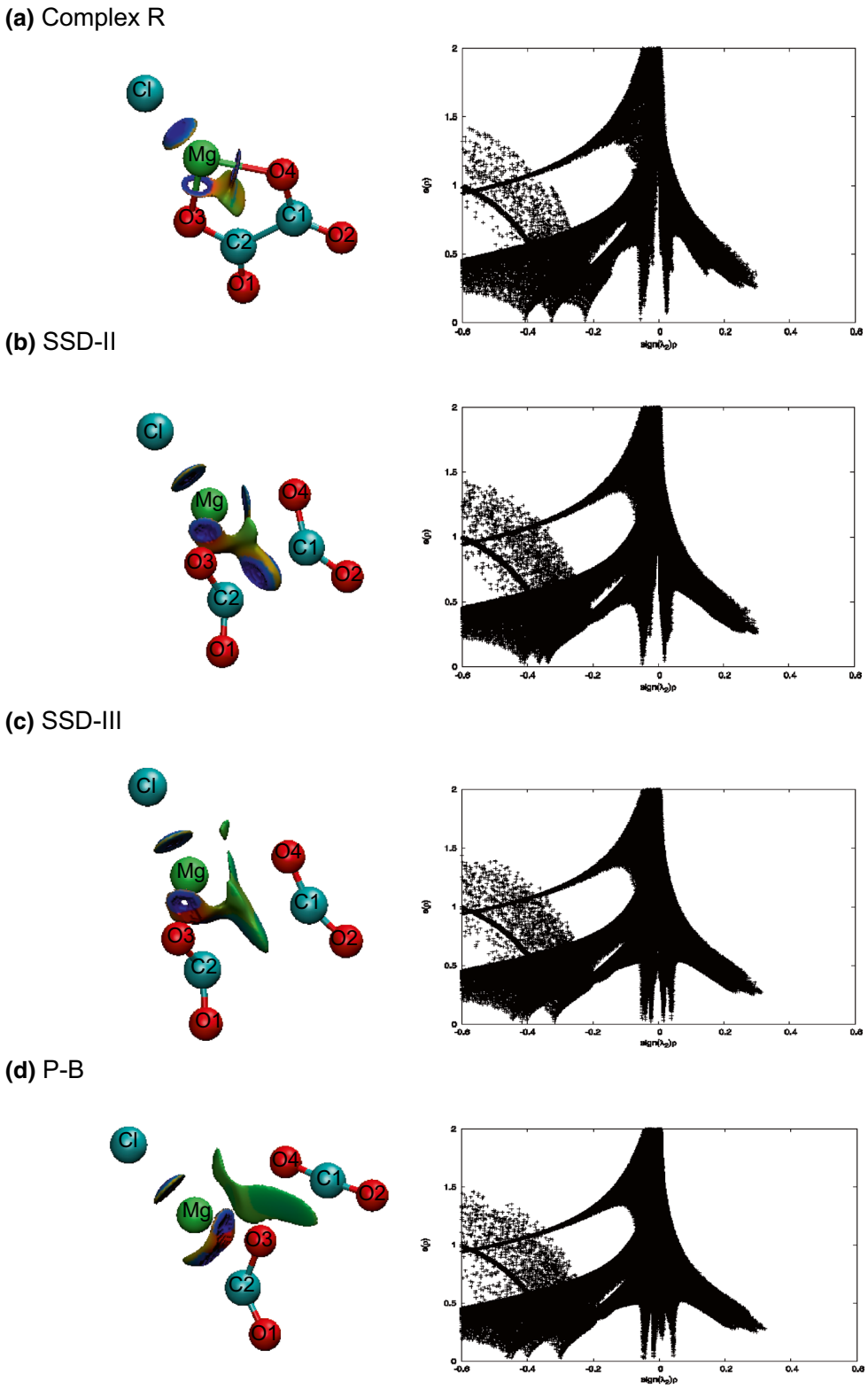

Fig. 4 Plots of the reduced density gradient versus the electron density multiplied by the sing of the second Hessian eigenvalue $\rho(r)(\lambda_2)$ and the respective reduced gradient isosurfaces

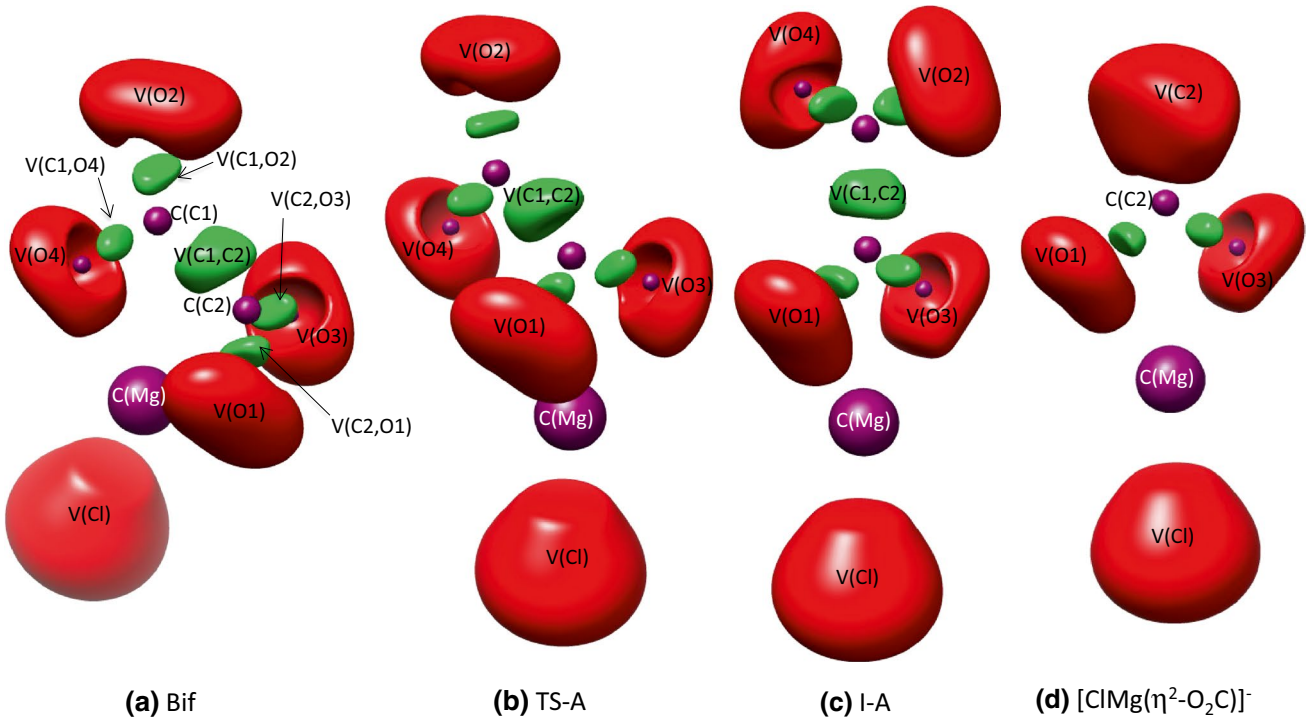

Fig. 5 Snapshots of the ELF localization domain ($\eta = 0.814$ isosurface) for Bif, TS-A, I-A, and $[ClMg(\eta^2\text{-}O_2C)]^-$. The *color code* is as follows: *green* disynaptic basins; *red* monosynaptic basins; *purple* core basins

4 Conclusions

The combined use of ELF, QTAIM, and NCI within QCT framework is a useful tool for studying the mechanisms of chemical reactions through the evolution of the topology of these three gradient fields, allowing the characterization of the electron redistribution in the course of a given chemical reaction.

The electronic structure and rearrangements of anionic $[ClMg(\eta^2\text{-}O_2C)]^-$ and $[ClMg(\eta^2\text{-}CO_2)]^-$ complexes have been elucidated, and the results obtained from this quantum chemical topological study allow to identify the evolution of strong and weak interactions among Mg and O and C atoms, recovering the electron flows and bonding patterns along the reaction pathways connecting these complexes. The reaction mechanisms for the rearrangements of anionic $[ClMg(\eta^2\text{-}O_2C)]^-$ and $[ClMg(\eta^2\text{-}CO_2)]^-$ complexes were rationalized in terms of chemical events that drive the chemical reaction and provides substantial information about chemical bonding along the reaction pathway, and allows us to investigate in detail the corresponding reaction pathways and to understand the flow of electrons that attends the process. Thus, the main reason for the preference of the system for the formation of **I-A** instead of **P-B** is reflected in the evolution of the population of the disynaptic basin V(C1,C2). The formation of **P-B** entails a collapse of the disynaptic basin V(C1,C2) due to an excess of charge density making the formation of **P-B** energetically more demanding and consequently a route kinetically less favorable. The conversion of **R** into **I-A** does not accounts for any breaking/forming process, and therefore, to overcome the energy barrier associated with **TS-A** makes this route significantly preferred.

Acknowledgements The authors are grateful to Generalitat Valenciana for PrometeoII/2014/022 and ACOMP/2015/1202, and Ministerio de Economía y Competitividad (Spain) for Project CTQ2015-65207-P. J.A and V.S are also grateful to Universitat Jaume I for Project P1·1B2013-40; M.O. is grateful to Universitat Jaume I for Project P1·1B2013-58. The authors are also grateful to the Servei d'Informàtica, Universitat Jaume I, for generous allocation of computer time.

References

1. Olah GA (2005) Beyond oil and gas: the methanol economy. Angew Chem Int Ed 44(18):2636–2639. doi:10.1002/anie.200462121
2. Webb JR, Bolano T, Gunnoe TB (2011) Catalytic oxy-functionalization of methane and other hydrocarbons: fundamental advancements and new strategies. Chemsuschem 4(1):37–49. doi:10.1002/cssc.201000319
3. Wang W, Wang S, Ma X, Gong J (2011) Recent advances in catalytic hydrogenation of carbon dioxide. Chem Soc Rev 40(7):3703–3727. doi:10.1039/c1cs15008a

4. Cokoja M, Bruckmeier C, Rieger B, Herrmann WA, Kuehn FE (2011) Transformation of carbon dioxide with homogeneous transition-metal catalysts: a molecular solution to a global challenge? Angew Chem Int Ed 50(37):8510–8537. doi:10.1002/anie.201102010
5. Olah GA (2013) Towards oil independence through renewable methanol chemistry. Angew Chem Int Ed 52(1):104–107. doi:10.1002/anie.201204995
6. Reddy PVL, Kim K-H, Song H (2013) Emerging green chemical technologies for the conversion of CH_4 to value added products. Renew Sustain Energy Rev 24:578–585. doi:10.1016/j.rser.2013.03.035
7. Aresta M, Dibenedetto A, Angelini A (2014) Catalysis for the valorization of exhaust carbon: from CO_2 to chemicals, materials, and fuels. Technological use of CO_2. Chem Rev 114(3):1709–1742. doi:10.1021/cr4002758
8. Weber JM (2014) The interaction of negative charge with carbon dioxide–insight into solvation, speciation and reductive activation from cluster studies. Int Rev Phys Chem 33(4):489–519. doi:10.1080/0144235x.2014.969554
9. Arakawa H, Aresta M, Armor JN, Barteau MA, Beckman EJ, Bell AT, Bercaw JE, Creutz C, Dinjus E, Dixon DA, Domen K, DuBois DL, Eckert J, Fujita E, Gibson DH, Goddard WA, Goodman DW, Keller J, Kubas GJ, Kung HH, Lyons JE, Manzer LE, Marks TJ, Morokuma K, Nicholas KM, Periana R, Que L, Rostrup-Nielson J, Sachtler WMH, Schmidt LD, Sen A, Somorjai GA, Stair PC, Stults BR, Tumas W (2001) Catalysis research of relevance to carbon management: progress, challenges, and opportunities. Chem Rev 101(4):953–996. doi:10.1021/cr000018s
10. Aresta M, Dibenedetto A (2007) Utilisation of CO_2 as a chemical feedstock: opportunities and challenges. Dalton Trans 28:2975–2992. doi:10.1039/b700658f
11. Schrader B (2002) Eur Environ 12:173–184
12. Firouzbakht M, Schlangen M, Kaupp M, Schwarz H (2016) Mechanistic aspects of CO_2 activation mediated by phenyl yttrium cation: a combined experimental/theoretical study. J Catal 343:68–74. doi:10.1016/j.jcat.2015.09.012
13. Firouzbakht M, Rijs NJ, Gonzalez-Navarrete P, Schlangen M, Kaupp M, Schwarz H (2016) On the activation of methane and carbon dioxide by $[HTaO]^+$ and $[TaOH]^+$ in the gas phase: a mechanistic study. Chem Eur J 22(30):10581–10589. doi:10.1002/chem.201601339
14. Li J, Gonzalez-Navarrete P, Schlangen M, Schwarz H (2015) Activation of methane and carbon dioxide mediated by transition-metal doped magnesium oxide clusters $[MMgO]^{+/0/-}$ (M = Sc–Zn). Chem Eur J 21(21):7780–7789. doi:10.1002/chem.201500715
15. Tang S-Y, Rijs NJ, Li J, Schlangen M, Schwarz H (2015) Ligand-controlled CO_2 activation mediated by cationic titanium hydride complexes, $[LTiH]^+$ (L = Cp_2, O). Chem Eur J 21(23):8483–8490. doi:10.1002/chem.201500722
16. Schwarz H (2017) Metal-mediated activation of carbon dioxide in the gas phase: mechanistic insight derived from a combined experimental/computational approach. Coord Chem Rev 334:112–123. doi:10.1016/j.ccr.2016.03.009
17. Rollason RJ, Plane JMC (2001) A kinetic study of the reactions of MgO with H_2O, CO_2 and O_2: implications for magnesium chemistry in the mesosphere. Phys Chem Chem Phys 3(21):4733–4740. doi:10.1039/b105673p
18. Schwach P, Willinger MG, Trunschke A, Schloegl R (2013) Methane coupling over magnesium oxide: how doping can work. Angew Chem Int Ed 52(43):11381–11384. doi:10.1002/anie.201305470
19. Kwapien K, Sierka M, Doebler J, Sauer J (2010) Reactions of H_2, CH_4, C_2H_6, and C_3H_8 with $[(MgO)_n]^+$ clusters studied by density functional theory. Chemcatchem 2(7):819–826. doi:10.1002/cctc.201000118
20. García V, Fernandez JJ, Ruiz W, Mondragon F, Moreno A (2009) Effect of MgO addition on the basicity of Ni/ZrO_2 and on its catalytic activity in carbon dioxide reforming of methane. Catal Commun 11(4):240–246. doi:10.1016/j.catcom.2009.10.003
21. Bouarab R, Akdim O, Auroux A, Cherifi O, Mirodatos C (2004) Effect of MgO additive on catalytic properties of Co/SiO_2 in the dry reforming of methane. Appl Catal A Gen 264(2):161–168. doi:10.1016/j.apcata.2003.12.039
22. Hu CW, Yang HQ, Wong NB, Chen YQ, Gong MC, Tian AM, Li C, Li WK (2003) Theoretical study on the mechanism of the reaction of CH_4 + MgO. J Phys Chem A 107(13):2316–2323. doi:10.1021/jp021953h
23. Nibbelke RH, Scheerova J, Decroon M, Marin GB (1995) The oxidative coupling of methane over Mg-based catalysts: a steady-state isotope transient kinetic analysis. J Catal 156(1):106–119. doi:10.1006/jcat.1995.1236
24. Jang W-J, Jeong D-W, Shim J-O, Roh H-S, Son IH, Lee SJ (2013) H_2 and CO production over a stable Ni–MgO–Ce0.8Zr0.2O2 catalyst from CO_2 reforming of CH_4. Int J Hydrogen Energy 38(11):4508–4512. doi:10.1016/j.ijhydene.2013.01.196
25. Zhang J, Wang H, Dalai AK (2009) Kinetic studies of carbon dioxide reforming of methane over Ni–Co/Al–Mg–O bimetallic catalyst. Ind Eng Chem Res 48(2):677–684. doi:10.1021/ie801078p
26. Wang HY, Ruckenstein E (2001) CO_2 reforming of CH_4 over Co/MgO solid solution catalysts—effect of calcination temperature and Co loading. Appl Catal A Gen 209(1–2):207–215. doi:10.1016/s0926-860x(00)00753-5
27. Aika K, Nishiyama T (1988) Utilisation of CO_2 in the oxidative coupling of methane over PbO–MgO and PbO–CaO. J Chem Soc Chem Commun 1:70–71. doi:10.1039/c39880000070
28. Teramura K, Tanaka T, Ishikawa H, Kohno Y, Funabiki T (2004) Photocatalytic reduction of CO_2 to CO in the presence of H_2 or CH_4 as a reductant over MgO. J Phys Chem B 108(1):346–354. doi:10.1021/jp0362943
29. Ellis RJ (1979) Most abundant protein in the world. Trends Biochem Sci 4(11):241–244. doi:10.1016/0968-0004(79)90212-3
30. Andersson I (2008) Catalysis and regulation in Rubisco. J Exp Bot 59(7):1555–1568. doi:10.1093/jxb/ern091
31. Grignard V (1901) Mixed organic magnesium combinations and their application to syntheses of acids, alcohols and hydrocarbons. Ann Chim Phys 24:433–490
32. Kwapien K, Paier J, Sauer J, Geske M, Zavyalova U, Horn R, Schwach P, Trunschke A, Schloegl R (2014) Sites for methane activation on lithium-doped magnesium oxide surfaces. Angew Chem Int Ed 53(33):8774–8778. doi:10.1002/anie.201310632
33. Cotton FA, Wilkinson G, Murillo CA, Bochmann M (1999) Advanced inorganic chemistry, 6th edn. Wiley, New York
34. Boese AD, Schneider H, Gloss AN, Weber JM (2005) The infrared spectrum of Au-CO_2. J Chem Phys. doi:10.1063/1.1875114
35. Knurr BJ, Weber JM (2013) Solvent-mediated reduction of carbon dioxide in anionic complexes with silver atoms. J Phys Chem A 117(41):10764–10771. doi:10.1021/jp407646t
36. Knurr BJ, Weber JM (2014) Infrared spectra and structures of anionic complexes of cobalt with carbon dioxide ligands. J Phys Chem A 118(23):4056–4062. doi:10.1021/jp503194v
37. Yeh CS, Willey KF, Robbins DL, Pilgrim JS, Duncan MA (1993) Photodissociation spectroscopy of the Mg^+–CO_2 complex ant its isotopic analogs. J Chem Phys 98(3):1867–1875. doi:10.1063/1.464221
38. Walters RS, Brinkmann NR, Schaefer HF, Duncan MA (2003) Infrared photodissociation spectroscopy of mass-selected $Al^+(CO_2)_n$ and $Al^+(CO_2)_nAr$ clusters. J Phys Chem A 107(38):7396–7405. doi:10.1021/jp030491k

39. Jaeger JB, Jaeger TD, Brinkmann NR, Schaefer HF, Duncan MA (2004) Infrared photodissociation spectroscopy of $Si^+(CO_2)_n$ and $Si^+(CO_2)_nAr$ complexes—evidence for unanticipated intracluster reactions. Can J Chem 82(6):934–946. doi:10.1139/v04-044
40. Walker NR, Walters RS, Duncan MA (2004) Infrared photodissociation spectroscopy of $V^+(CO_2)_n$ and $V^+(CO_2)_nAr$ complexes. J Chem Phys 120(21):10037–10045. doi:10.1063/1.1730217
41. Gregoire G, Duncan MA (2002) Infrared spectroscopy to probe structure and growth dynamics in Fe^+-$(CO_2)_n$ clusters. J Chem Phys 117(5):2120–2130. doi:10.1063/1.1490600
42. Walker NR, Walters RS, Grieves GA, Duncan MA (2004) Growth dynamics and intracluster reactions in $Ni^+(CO_2)_n$ complexes via infrared spectroscopy. J Chem Phys 121(21):10498–10507. doi:10.1063/1.1806821
43. Asher RL, Bellert D, Buthelezi T, Brucat PJ (1994) The $CO + CO_2$ electrostatic complex: geometry and potential. Chem Phys Lett 227(6):623–627. doi:10.1016/0009-2614(94)00890-6
44. Miller GBS, Esser TK, Knorke H, Gewinner S, Schoellkopf W, Heine N, Asmis KR, Uggerud E (2014) Spectroscopic identification of a bidentate binding motif in the anionic magnesium–CO_2 complex ($[ClMgCO_2]^-$). Angew Chem Int Ed 53(52):14407–14410. doi:10.1002/anie.201409444
45. Popelier PLA, Bremond EAG (2009) Geometrically faithful homeomorphisms between the electron density and the bare nuclear potential. Int J Quantum Chem 109(11):2542–2553. doi:10.1002/qua.22215
46. Krokidis X, Noury S, Silvi B (1997) Characterization of elementary chemical processes by catastrophe theory. J Phys Chem A 101(39):7277–7282
47. González-Navarrete P, Domingo LR, Andrés J, Berski S, Silvi B (2012) Electronic fluxes during diels-alder reactions involving 1,2-benzoquinones: mechanistic insights from the analysis of electron localization function and catastrophe theory. J Comput Chem 33(30):2400–2411
48. Andres J, Berski S, Domingo LR, Gonzalez-Navarrete P (2012) Nature of the ring-closure process along the rearrangement of octa-1,3,5,7-tetraene to cycloocta-1,3,5-triene from the perspective of the electron localization function and catastrophe theory. J Comput Chem 33(7):748–756. doi:10.1002/jcc.22898
49. Santos JC, Andres J, Aizman A, Fuentealba P, Polo V (2005) A theoretical study on the reaction mechanism for the Bergman cyclization from the perspective of the electron localization function and catastrophe theory. J Phys Chem A 109(16):3687–3693. doi:10.1021/jp0441947
50. Polo V, Gonzalez-Navarrete P, Silvi B, Andres J (2008) An electron localization function and catastrophe theory analysis on the molecular mechanism of gas-phase identity S_N2 reactions. Theoret Chem Acc 120(4–6):341–349. doi:10.1007/s00214-008-0427-6
51. Becke AD, Edgecombe KE (1990) A simple measure of electron localization in atomic and molecular systems. J Chem Phys 92:5397–5403
52. Silvi B, Savin A (1994) Classification of chemical bonds based on topological analysis of electron localization functions. Nature 371:683–686
53. Thom R (1976) Structural stability and morphogenesis. W. A. Benjamin Inc., Redding
54. Bader RFW (1990) Atoms in molecules: a quantum theory. Oxford University Press, Oxford
55. Johnson ER, Keinan S, Mori-Sánchez P, Contreras-García J, Cohen AJ, Yang W (2010) Revealing noncovalent interactions. J Am Chem Soc 132(18):6498–6506
56. Andres J, Berski S, Contreras-Garcia J, Gonzalez-Navarrete P (2014) Following the molecular mechanism for the $NH_3 + LiH \rightarrow LiNH_2 + H_2$ chemical reaction: a study based on the joint use of the quantum theory of atoms in molecules (QTAIM) and noncovalent interaction (NCI) index. J Phys Chem A 118(9):1663–1672. doi:10.1021/jp4111376
57. Contreras-García J, Yang W, Johnson ER (2011) Analysis of hydrogen-bond interaction potentials from the electron density: integration of noncovalent interaction regions. J Phys Chem A 115(45):12983–12990
58. Alonso M, Woller T, Martín-Martínez FJ, Contreras-García J, Geerlings P, De Proft F (2014) Understanding the fundamental role of π/π, σ/σ, and σ/π dispersion interactions in shaping carbon-based materials. Chem A Eur J 20(17):4845. doi:10.1002/chem.201400428
59. Lane JR, Contreras-García J, Piquemal J-P, Miller BJ, Kjaergaard HG (2013) Are bond critical points really critical for hydrogen bonding? J Chem Theor Comput 9(8):3263–3266
60. Boto RA, Contreras-Garcia J, Calatayud M (2015) The role of dispersion forces in metal-supported self-assembled monolayers. Comput Theor Chem 1053:322–327. doi:10.1016/j.comptc.2014.10.015
61. Frisch MJ, Trucks GW, Schlegel HB, Scuseria GE, Robb MA, Cheeseman JR, Scalmani G, Barone V, Mennucci B, Petersson GA, Nakatsuji H, Caricato M, Li X, Hratchian HP, Izmaylov AF, Bloino J, Zheng G, Sonnenberg JL, Hada M, Ehara M, Toyota K, Fukuda R, Hasegawa J, Ishida M, Nakajima T, Honda Y, Kitao O, Nakai H, Vreven T, Montgomery JA, Jr, Peralta JE, Ogliaro F, Bearpark M, Heyd JJ, Brothers E, Kudin KN, Staroverov VN, Kobayashi R, Normand J, Raghavachari K, Rendell A, Burant JC, Iyengar SS, Tomasi J, Cossi M, Rega N, Millam NJ, Klene M, Knox JE, Cross JB, Bakken V, Adamo C, Jaramillo J, Gomperts R, Stratmann RE, Yazyev O, Austin AJ, Cammi R, Pomelli C, Ochterski JW, Martin RL, Morokuma K, Zakrzewski VG, Voth GA, Salvador P, Dannenberg JJ, Dapprich S, Daniels AD, Farkas Ö, Foresman JB, Ortiz JV, Cioslowski J, Fox DJ (2010) Gaussian 09 RB Inc., Wallingford CT
62. Becke AD (1993) Density-functional thermochemistry. III. The role of exact exchange. J Chem Phys 98:5648–5652
63. Lee C, Yang W, Parr RG (1988) Development of the Colle–Salvetti correlation-energy formula into a functional of the electron density. Phys Rev B 37(2):785–789
64. Fukui K (1970) A formulation of reaction coordinate. J Phys Chem 74(23):4161–4163. doi:10.1021/j100717a029
65. Fukui K (1981) The path of chemical-reactions—the IRC approach. Acc Chem Res 14(12):363–368. doi:10.1021/ar00072a001
66. Noury S, Krokidis X, Fuster F, Silvi B (1999) Computational tools for the electron localization function topological analysis. Comput Chem 23(6):597–604. doi:10.1016/s0097-8485(99)00039-x
67. Pettersen EF, Goddard TD, Huang CC, Couch GS, Greenblatt DM, Meng EC, Ferrin TE (2004) UCSF chimera—a visualization system for exploratory research and analysis. J Comput Chem 25(13):1605–1612. doi:10.1002/jcc.20084
68. Silvi B (2002) The synaptic order: a key concept to understand multicenter bonding. J Mol Struct 614(1–3):3–10. doi:10.1016/s0022-2860(02)00231-4
69. Gillet N, Chaudret R, Contreras-García J, Yang W, Silvi B, Piquemal J-P (2012) Coupling quantum interpretative techniques: another look at chemical mechanisms in organic reactions. J Chem Theor Comput 8(11):3993–3997
70. Andres J, Gracia L, Gonzalez-Navarrete P, Safont VS (2015) Chemical structure and reactivity by means of quantum chemical topology analysis. Comput Theor Chem 1053:17–30. doi:10.1016/j.comptc.2014.10.010

71. Andrés J, González-Navarrete P, Safont VS (2014) Unraveling reaction mechanisms by means of quantum chemical topology analysis. Int J Quantum Chem 114(9):1239–1252. doi:10.1002/qua.24665
72. Lu T, Chen F (2012) Multiwfn: a multifunctional wavefunction analyzer. J Comput Chem 33(5):580–592. doi:10.1002/jcc.22885
73. Contreras-García J, Johnson ER, Keinan S, Chaudret R, Piquemal J-P, Beratan DN, Yang W (2011) NCIPLOT: a program for plotting noncovalent interaction regions. J Chem Theor Comput 7(3):625–632